Pergamon

J. Mech. Phys. Solids, Vol. 42, No. 11, pp. 1653–1677, 1994

0022–5096/94 $7.00+0.00

0022–5096(94)00052–2

EMERGENCE OF CRACKS BY MASS TRANSPORT IN ELASTIC CRYSTALS STRESSED AT HIGH TEMPERATURES

B. SUN, Z. SUO and A. G. EVANS

Mechanical and Environmental Engineering Department, Materials Department, University of California, Santa Barbara, CA 93106, U.S.A.

(*Received* 10 *June* 1994; *in revised form* 11 *July* 1994)

ABSTRACT

Single crystals are used under high temperatures and high stresses in hostile environments (usually gases). A void produced in the fabrication process can change shape and volume, as atoms migrate under various thermodynamic forces. A small void under low stress remains rounded in shape, but a large void under high stress evolves to a crack. The material fractures catastrophically when the crack becomes sufficiently large. In this article three kinetic processes are analyzed: diffusion along the void surface, diffusion in a low melting point second phase inside the void, and surface reaction with the gases. An approximate evolution path is simulated, with the void evolving as a sequence of spheroids, from a sphere to a penny-shaped crack. The free energy is calculated as a functional of void shape, from which the instability conditions are determined. The evolution rate is calculated by using variational principles derived from the balance of the reduction in the free energy and the dissipation in the kinetic processes. Crystalline anisotropy and surface heterogeneity can be readily incorporated in this energetic framework. Comparisons are made with experimental strength data for sapphire fibers measured at various strain rates.

1. INTRODUCTION

Inorganic solids stressed at elevated temperatures often fail by creep deformation and rupture. These processes involve diffusion along grain boundaries and dislocation cell boundaries, motivated by applied stresses. They have been comprehensively studied (Chan and Page, 1993). The usual approach to enhancing creep resistance is to fabricate materials with large grains. The limiting case involves single crystals, exemplified by superalloys used for turbine blades and oxides used for fiber reinforcements. Diffusional phenomena also limit the performance of these materials. However, the appropriate mechanisms have not been established. The intent of this article is to provide an analysis of time-dependent rupture mechanisms that occur in single crystals.

The rationale for the choice of mechanisms is provided by measurements and observations of high temperature rupture of single crystal aluminum oxide (sapphire) fibers. Newcomb and Tressler (1993) demonstrated that, when stressed at high temperatures, cracks originate from internal pores, grow slowly at first and, upon attaining a critical size, cause catastrophic fracture. We suggest a mechanism sketched in Fig.

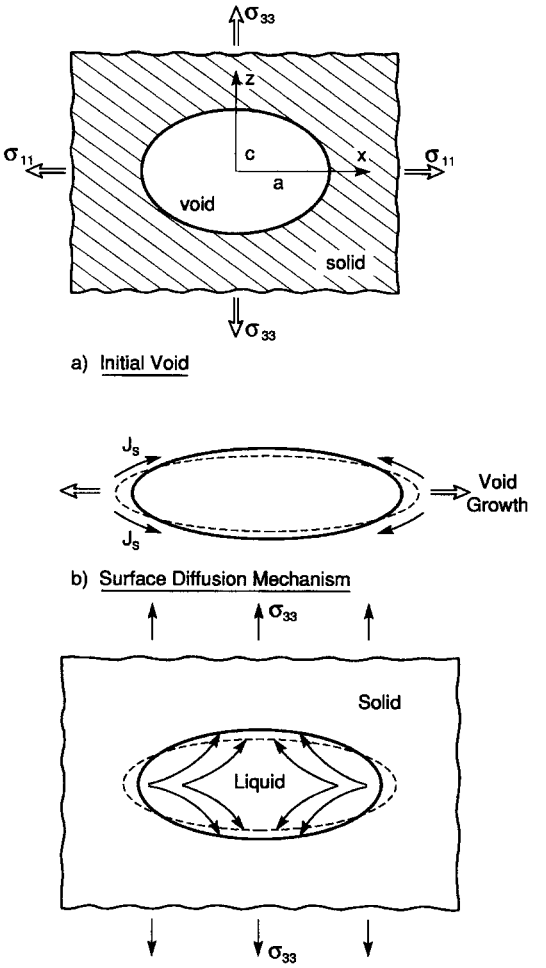

Fig. 1. (a) The cross-section of a spheroidal void in an infinite solid. (b) A void changes shape by surface diffusion. (c) A void filled with a liquid that provides a fast diffusion path.

1. Motivated by the applied stress, atoms diffuse on the void surface, changing the void shape from a sphere to a crack [Fig. 1(b)]. Such crack growth is accelerated if a fluid (either liquid or gas) exists within the crack. This mechanism has two features: (i) it provides a path for rapid mass relocation [Fig. 1(c)]; (ii) the solid and fluid may chemically react, leading to dissolution and reprecipitation along the void surface. Each of these kinetic processes is analyzed in this article. A comparison with experimental data is then made.

It appears that stress-induced mass transport in elastic solids was first studied by Asaro and Tiller (1972) and by Stevens and Dutton (1971). Asaro and Tiller studied the stability of a flat surface of a stressed solid against surface diffusion. Their linear

stability analysis showed that a slight undulation of the surface decays if the surface energy dominates, but amplifies itself if the elastic energy dominates. They suggested that the positive feedback in the latter case would lead to surface cracks. The same instability has been rediscovered by Grinfel'd (1986, 1993), Srolovitz (1989) and Gao (1991), and found particular relevance in thin epitaxial films (Spencer *et al.*, 1991; Freund and Jonsdottir, 1993). Nonlinear analyses of Chiu and Gao (1993) and Yang and Srolovitz (1993) have confirmed that cracks will emerge from the surface undulation. The same concepts apply to the instability of cylindrical voids in elastic solids (Stevens and Dutton, 1971; Gao, 1992, 1993; Suo and Wang, 1994).

Building upon these previous investigations, this article will study the evolution of a three dimensional void, with the kinetic processes significant to single crystals used as structural components. The free energy is computed as a functional of the void shape. The free energy landscape determines the instability conditions. The method of Suo and Wang (1994) will be adopted to study the kinetics. In this method, evolution is traced by using variational principles that govern the rates. The functionals to be minimized involve the rate of reduction in the free energy and the rate of dissipation associated with the kinetic processes. The energetics of these problems are examined first, followed by analysis of the kinetics for the three mechanisms. Both the energetics and kinetics differ for the diffusion and the reaction problems. They will be analyzed separately.

2. ENERGETICS OF VOID INSTABILITY

2.1. *Diffusion problem*

Sketched in Fig. 1(a) is a void in an infinite elastic solid having the cross-section in the (X, Z) plane. An axially symmetric problem will be analyzed in which the void evolves as a sequence of oblate spheroids. The three semi-axes satisfy $a = b \geqslant c$ and the solid is under a remote triaxial stress state $\sigma_{11} = \sigma_{22} \leqslant \sigma_{33}$. For the diffusion problem, the void changes shape but volume is conserved. The volume-conserving spheroids are described by

$$X = a_0 \alpha \cos\theta, \quad Z = a_0 \alpha^{-2} \sin\theta. \tag{2.1}$$

Here a_0 is the radius of a sphere having the same volume as the void and is independent of the time. The shape parameter, α, evolves with the time; $\alpha = 1$ corresponds to a sphere and $\alpha \to \infty$ corresponds to a penny-shaped crack. At a fixed time, (2.1) traces the entire ellipse on the (X, Z) plane as θ varies in the interval $(0, 2\pi)$.

When a traction-free void is introduced, the body becomes more compliant and the remote stress does work. The *increase* in the strain energy upon introducing a spheroidal void to an infinite solid, U_E, scales with the void volume and the strain energy density:

$$U_E = \frac{4\pi a_0^3 \sigma_{33}^2}{3E} B, \tag{2.2}$$

where E is Young's modulus. The dimensionless coefficient B is listed in Appendix A,

which depends on the shape parameter α, the stress ratio $k = \sigma_{11}/\sigma_{33}$ and Poisson's ratio ν ($= 1/3$ in the numerical calculations). If the surface tension, γ_0, is isotropic, the change in the surface energy upon introducing the void, U_S, is γ_0 times the total surface area of the spheroid

$$U_S = 4\pi a_0^2 \gamma_0 A_0. \tag{2.3}$$

The dimensionless number A_0, which depends on α, is listed in Appendix A. Also note that the applied work is twice the stored elastic energy. Upon introducing the void into the stressed solid, the net change in the free energy is

$$\Phi = U_S - U_E. \tag{2.4}$$

This free energy is a functional of the void shape. To reduce Φ, atoms relocate on the void surface, resulting in the change of the void shape. This competition between the elastic energy and the surface energy also appeared in Griffith's analysis of crack growth, although there the free energy is a functional of the crack size, which grows as atomic bonds break at the crack front—no long range mass transport is involved.

A comparison between (2.2) and (2.3) defines a dimensionless number,

$$\Lambda = \frac{\sigma_{33}^2 a_0}{\gamma_0 E}, \tag{2.5}$$

which measures the relative significance of the elastic energy and the surface energy. When Λ is small, the surface energy dominates and the void tends to spheroidize. When Λ is large, the elastic energy dominates and the void tends to collapse into a crack. The void radius appears in (2.5) because U_E scales with the void volume, but U_S scales with the void surface. The physical origin of this instability is understood as follows. A spherical void under hydrostatic stress is in equilibrium: no unbalanced force drives surface diffusion. Yet this equilibrium can be unstable. When the sphere is slightly perturbed to become a spheroid, both U_S and U_E increase because the surface area and the compliance both increase. If the perturbation increases U_S more than U_E, the surface energy restores the spherical symmetry. If the perturbation increases U_S less than U_E the strain energy amplifies the perturbation and the void collapses into a crack.

These points are quantitatively displayed in Fig. 2, where $\Delta\Phi$ is the free energy difference between a spheroid and a sphere. For convenience, we have defined another shape parameter m by

$$\alpha = \left(\frac{1+m}{1-m}\right)^{1/2} - 1. \tag{2.6}$$

The sphere corresponds to $m = 0$ and the penny-shaped crack to $m = 1$. Each curve on Fig. 2 corresponds to a fixed Λ. A minimum or a maximum represents a stable or an unstable equilibrium state, respectively. Three behaviors are possible depending on the level of Λ: (1) When $\Lambda = 0$ (no stress is applied), Φ reaches a minimum at $m = 0$ and a maximum at $m = 1$. The spherical void is stable and the crack is unstable. Any spheroid relaxes to a sphere. (2) When $0 < \Lambda < 16/9$ (for example, $\Lambda = 3/8$ in the figure), the stress is finite but surface energy still dominates; Φ reaches a local

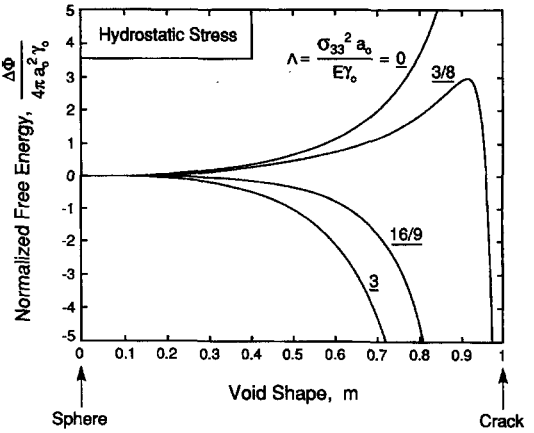

Fig. 2. The free energy difference between a spheroidal and spherical void, $\Delta\Phi$, as a function of void shape, m, at several fixed load levels, Λ. The body in under remote hydrostatic stress.

minimum at $m = 0$, a global maximum at a characteristic shape m_c, and a global minimum at $m = 1$. The maximum acts as an energy barrier. A spheroid having $m < m_c$ relaxes to a sphere, but a spheroid having $m > m_c$ collapses to a crack. (3) When $\Lambda > 16/9$ (for example, $\Lambda = 3$ in the figure), the stress dominates; Φ reaches a maximum at $m = 0$ and a minimum at $m = 1$. The sphere is unstable, but the crack is stable. Any void collapses to a crack. Moreover, for any imperfect system, such as a void subjected to biased triaxial stress, the spherical void will not be in equilibrium. The behavior is exemplified by Fig. 3, which shows the free energy for a void under uniaxial stress σ_{33}. As expected, under an intermediate loading level (for example, $\Lambda = 3/4$ in the figure), the spherical void does not minimize the free energy. The minimum is attained by a spheroid having finite m.

Equilibrium states under several remote stress states are plotted in the (Λ, m) space

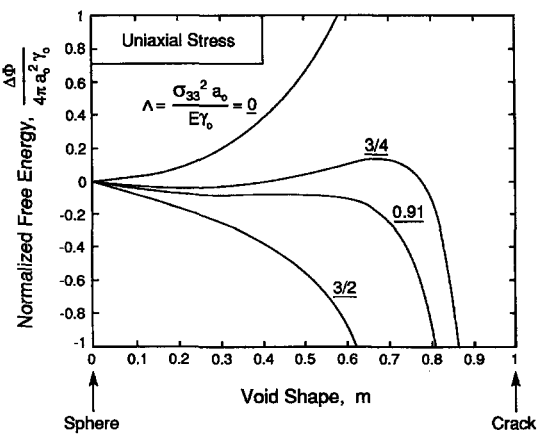

Fig. 3. The free energy difference between a spheroidal and spherical void, $\Delta\Phi$, as a function of void shape, m, at several fixed load levels, Λ. The body in under remote uniaxial stress.

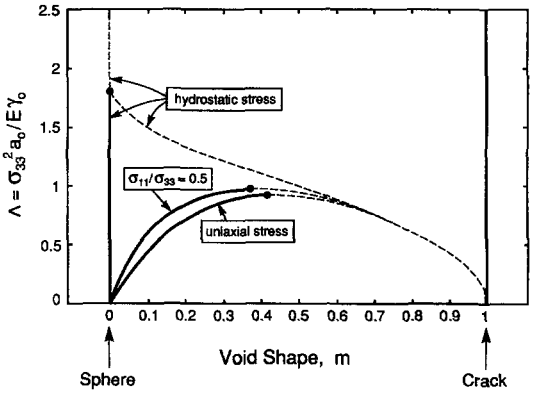

Fig. 4. A diagram of equilibrium states under several remote stress states. The solid lines represent stable equilibrium and the dashed lines represent unstable equilibrium.

on Fig. 4. The solid and the dotted lines correspond to the stable and the unstable equilibrium states, respectively. At a fixed loading level Λ, a point (Λ, m) that does not lie on the curve represents a nonequilibrium void, which will evolve toward a stable equilibrium state. Under hydrostatic stress and for small Λ, the spherical void is stable. The instability occurs at a *bifurcation point*, $\Lambda_c = 16/9$. Under uniaxial stress, the void assumes a spheroidal equilibrium shape for small Λ. The instability occurs at a *limit point*, $\Lambda_c = 0.91$. The equilibrium diagrams are quite different for the hydrostatic and the uniaxial stress states, but convey similar implications. A void settles to a rounded shape when Λ is small, but collapses to a crack when Λ is large.

Note that all curves in Fig. 4 merge to the same asymptote as $m \to 1$, corresponding to a penny-shaped crack of radius $a \approx a_0\alpha$. These energetics coincide with the Griffith condition for crack growth:

$$\frac{(1-\nu^2)\sigma_{33}^2 a}{E\gamma_0} = \frac{\pi}{2}, \tag{2.7}$$

assuming that the fracture energy is $2\gamma_0$. This condition is independent of the stress component σ_{11}. Consequently, all curves in Fig. 4 have the identical asymptote.

A plot of the limit points Λ_c as a function of the stress ratio σ_{11}/σ_{33} (Fig. 5) demonstrates that a void collapses to a crack if subjected to a loading level above the curve, but remains rounded if subjected to a loading level below the curve. The basic trends are the same when surface energy is anisotropic, as shown in Appendix B.

2.2. *Surface reactions*

The surface reaction problem differs from the diffusion problem because (1) both the void shape and volume can change, and (2) the free energy due to the reaction must be added. These differences are explained in this section. Imagine that the solid reacts with a mixture of gases over the surface of the void. The gases may be present either inside an internal pore, or over a pore on the external void surface. The thermal conductivity is taken to be sufficiently large, so that *thermal equilibrium* is quickly

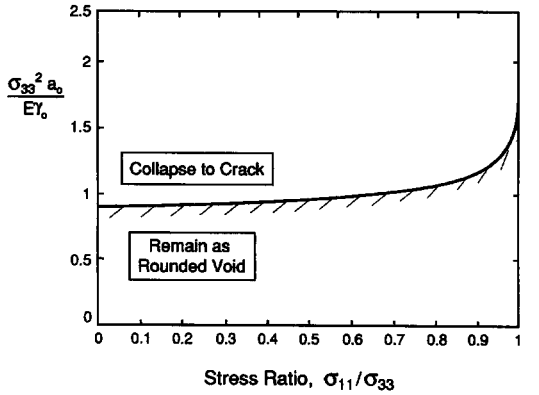

Fig. 5. The limit load Λ_c as a function of remote stress state.

established and the system is under a uniform temperature T. Also assume that diffusion in the gas mixture is fast so that *mechanical equilibrium* is quickly established. Thus, each gas species has a uniform partial pressure p_i. It is the kinetic process taking place in the thin boundary layer immediately over the solid surface that limits the void evolution rate. We approximate the void shape by a spheroid

$$X = a\cos\theta, \quad Z = c\sin\theta. \tag{2.8}$$

The semi-axes a and c both change with the time. This differs from the diffusion problem, where the void volume is conserved.

Denote μ_s^0 as the chemical potential (per molecule) of the unstressed solid, which is to a good approximation unchanged by the gas pressure. Denote μ_i^0 as the chemical potential of gas i at a reference pressure p^0. At partial pressure p_i, gas i has the chemical potential

$$\mu_i = \mu_i^0 + kT\ln(p_i/p^0). \tag{2.9}$$

Here k is Boltzmann's constant. Both μ_s^0 and μ_i^0 are the values relevant at the temperature T.

For simplicity, the partial pressures, and therefore the chemical potentials, of the gases are assumed to be time-independent during the reaction. The solid is taken to be a reaction product with the stoichiometric coefficient being unity. The gas species i has stoichiometric coefficient ν_i—positive for products and negative for reactants. That is, to deposit one solid molecule, $\nu_i\xi$ molecules of gas i are produced. Due to the chemical reaction, introducing the void into the solid increases the free energy by

$$U_C = -\frac{4\pi a^2 c}{3\Omega}(\mu_s^0 + \sum \nu_i\mu_i), \tag{2.10}$$

where Ω is the volume per solid molecule and the ratio in front of the bracket is the number of the solid molecules that occupy the volume of the void. The net change in the free energy is

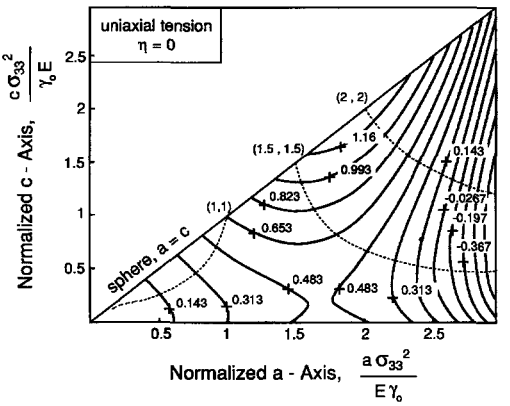

Fig. 6. Energy landscape and evolution path due to surface reactions. The solid lines are constant free energy contours. The dotted lines are evolution paths for several voids starting from spheres of different radii.

$$\Phi = U_S - U_E + U_C. \tag{2.11}$$

A comparison of U_E and U_C defines a dimensionless parameter,

$$\eta = \frac{E}{\sigma_{33}^2 \Omega}\left(\mu_s^0 + \sum \nu_i \mu_i\right), \tag{2.12}$$

which measures the relative importance of the chemical potential and the strain energy. The parameter is independent of void size, because both U_E and U_C scale with the void volume. The effect of the stress is negligible when either $\eta \gg +1$ or $\eta \ll -1$. For the former, the solid has very high chemical potential and dissolves from the surface. For the latter, the solid has very low chemical potential and precipitates onto the surface. In what follows we address the case $\eta \approx 0$, or $U_C \approx 0$. That is, a flat unstressed solid surface is approximately in equilibrium with its surrounding gases, but the equilibrium is disrupted when the solid surface is curved and stressed. Even in this case, the void changes both volume and shape, as a result of the competition between the surface energy U_S and the elastic energy U_E.

For further analysis, a length scale is defined as

$$\lambda = \gamma_0 E/\sigma_{33}^2. \tag{2.13}$$

The semi-axes a and c of the spheroid are normalized by λ. The free energy is normalized as $\Phi/(4\pi\lambda^2\gamma_0)$. Figure 6 shows the free energy contours in (a, c) space for an oblate spheroidal void under uniaxial tension σ_{33} and $\eta = 0$. The free energy surface, $\Phi(a, c)$, has a saddle point. The low potential is reached when the void is either a vanishingly small sphere or a large crack. These features are physically understood as follows. Under uniaxial stress, the elastic energy U_E and the surface energy U_S increase when the void either increases size or becomes an oblate spheroid. However, the two energies have different dependence on the length scale: U_E is proportional to the volume and U_S to the surface. Consequently, U_E determines the

behavior of large voids and U_S determines the behavior of small voids. Additional calculations show that the trends remain to be the same when $\eta = -1$ or $\eta = +1$.

3. CRACK GROWTH BY SURFACE DIFFUSION

Let $\mathbf{X}$ be the position vector of a point on the void surface, and $\mathbf{n}$ the unit vector normal to the void surface directed toward the solid. As solid molecules deplete or accumulate, a surface element moves at velocity

$$V_n = \mathbf{n} \cdot \dot{\mathbf{X}}. \tag{3.1}$$

The superimposed dot represents the time derivative. Denote J_s as the molecular flux on the surface (i.e. the number of molecules per time crossing unit length on the surface). Mass conservation requires that the surface velocity be related to the *divergence* of the flux:

$$V_n = \Omega \, \partial(X J_s)/(X \, \partial s), \tag{3.2}$$

where Ω is the volume per molecule and $\mathrm{d}s$ is the line element of the ellipse in the (X, Z) plane. Equations (2.1), (3.1) and (3.2) specify the kinematics of the evolution.

The kinetics are analyzed by defining a thermodynamic force per solid molecule, F. The equivalence of this approach with local chemical potential concepts has been demonstrated in Suo and Wang (1994). This force is defined as the reduction in the free energy associated with a molecule migrating unit distance. Thus,

$$\dot{\Phi} + \int F J_s \, \mathrm{d}S = 0 \tag{3.3}$$

for any virtual flux and velocity. The integral extends over the void surface. The first term in (3.3) is the rate of free energy change and the second term is the rate of dissipation associated with surface diffusion. That is, the free energy reduction is dissipated by diffusion.

The kinetics are specified in the usual manner:

$$J_s = M_s F, \tag{3.4}$$

where M_s is the surface mobility, which relates to the surface diffusivity $D_s\delta_s$ by the Einstein relation $M_s = D_s\delta_s/\Omega \mathrm{k}T$ (with $\mathrm{k}T$ playing the usual role). The mobility, and therefore the diffusivity, are determined experimentally by their macroscopic consequences, for example, by measuring the rate of thermal grooving.

The following variational principle is equivalent to the combination of (3.3) and (3.4). Among all virtual fluxes that satisfy the kinematics [(2.1), (3.1) and (3.2)], the *actual* flux minimizes the functional

$$\Pi = \dot{\Phi} + \int \frac{J_s^2}{2M_s} \mathrm{d}S. \tag{3.5}$$

That is, at each time step, Π is a functional of the flux distribution, to be minimized

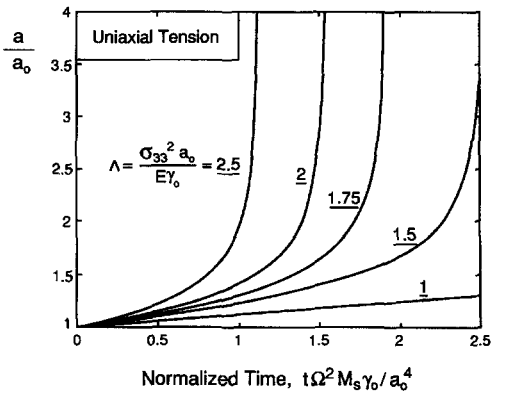

Fig. 7. Evolution of the semi-axis of a void due to surface diffusion.

for a fixed void shape. The velocity so determined updates the void shape. The process is repeated for many time steps.

For convenience, all geometric lengths are normalized by a_0. Then, by equating the dimensions of the two terms on the right-hand side of (3.5), we find a characteristic time t_0, given by

$$t_0 = \frac{a_0^4}{\Omega^2 M_s \gamma_0} \equiv \frac{a_0^4 kT}{\Omega D_s \delta_s \gamma_0}. \tag{3.6}$$

In the subsequent analysis, the time t is normalized by t_0.

For a void evolving as a sequence of spheroids, the surface velocity determined from (2.1) and (3.1) is

$$V_n = a_0^2 \alpha^{-2} \dot{\alpha} (\cos^2 \theta - 2 \sin^2 \theta)\, d\theta/ds. \tag{3.7}$$

An integration of (3.2) gives the flux

$$J_s = \frac{a_0^2}{2\Omega} \left(\frac{\dot{\alpha}}{\alpha^2} \right) \sin 2\theta. \tag{3.8}$$

The integration constant is set by the symmetry condition, $J_s = 0$ at $\theta = 0$. The functional Π, after normalization, becomes

$$\Pi = (-\Lambda I_0 + I_1)\dot{\alpha} + \tfrac{1}{2} I_2 \dot{\alpha}^2. \tag{3.9}$$

The coefficients I_i are functions of α; they are listed in Appendix A.

Minimizing Π by letting $\partial \Pi / \partial \dot{\alpha} = 0$ gives

$$\dot{\alpha} = (\Lambda I_0 - I_1)/I_2. \tag{3.10}$$

This nonlinear ordinary differential equation is numerically integrated to give the void shape as a function of time, Fig. 7. The loading levels Λ are above the limit load $\Lambda_c = 0.91$. Note that for $\Lambda > 1.75$, the void collapses to a crack within two units of the characteristic time, t_0.

Crack extension may also occur when loading is applied at a constant strain rate,

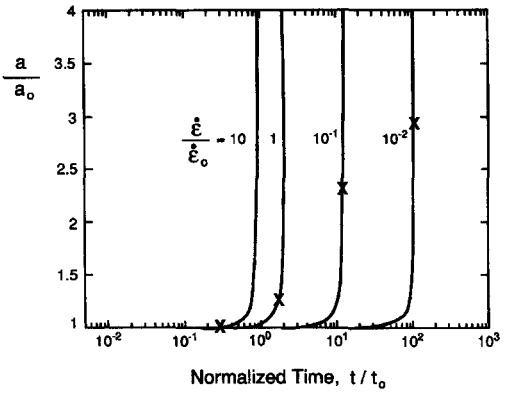

Fig. 8. Evolution of the semi-axis of a void loaded at various strain rates, assuming the change is solely caused by surface diffusion.

$\dot{\varepsilon}$, resulting in a fracture strength σ_c that increases with increase in $\dot{\varepsilon}$. To analyze this problem, consider an elastic solid stressed at a constant strain rate, so that the applied stress increases linearly with the time, $\sigma = E\dot{\varepsilon}t$. The dimensionless parameter defined by (2.5) becomes

$$\Lambda = \frac{(E\dot{\varepsilon}t)^2 a_0}{E\gamma_0} \equiv (\dot{\varepsilon}/\dot{\varepsilon}_0)^2 (t/t_0)^2, \tag{3.11}$$

where t_0 is defined by (3.6) and $\dot{\varepsilon}_0$ is defined by

$$\dot{\varepsilon}_0 = \left(\frac{\gamma_0}{Ea_0}\right)^{1/2} \frac{\Omega D_s \delta_s \gamma_0}{a_0^4 kT}. \tag{3.12}$$

The differential equation (3.10) is integrated to give the evolution of the semi-axis of the void loaded at several strain rates, Fig. 8. Subject to a given strain rate, the void shape remains almost unchanged until the applied stress is large enough. The void flattens rapidly after the stress exceeds the level corresponding to the limit point, $\Lambda_c = 0.91$.

To determine the critical semi-axis for fracture, a_c, we approximate the spheroid by a penny-shaped crack of the same radius a. The increase in the strain energy associated with unit crack front extending unit distance is (Tada *et al.*, 1985)

$$G = \frac{4(1-\nu^2)}{\pi E}\sigma^2 a. \tag{3.13}$$

Fracture occurs when the energy release rate reaches the fracture energy, G_c. The fracture conditions determined by assuming $G_c/\gamma_0 = 3.5$ are indicated in Fig. 8 by (X). The predicted strength, σ_c, as a function of the strain rate, $\dot{\varepsilon}$, is plotted on Fig. 9 in a normalized form.

4. CRACK GROWTH BY DIFFUSION WITHIN A FLUID MEDIUM

Consider a solid containing a void filled with a second phase which is a fluid at elevated temperatures, Fig. 1(c). Solid molecules dissolve at one location on the void

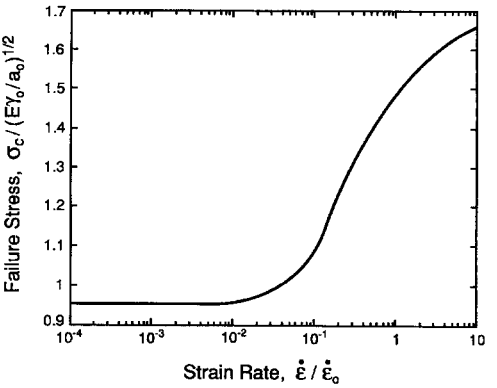

Fig. 9. Predicted strength at various strain rates plotted in a normalized form.

surface, diffuse through the fluid and then deposit at another location on the void surface, leading to the change in the void shape. Diffusion within the fluid is taken to limit the void evolution rate. The process is still driven by the competing forces due to the elastic energy and the surface energy.

Denote J_i as the molecular flux vector (the number of molecules passing unit area in unit time). Assume that the concentration of the atoms of the solid within the fluid phase has reached a steady state. Then, mass conservation requires the flux to be divergence-free in the fluid,

$$J_{i,i} = 0, \tag{4.1}$$

and that the flux relate to the velocity on the void surface by

$$V_n = -\Omega J_i n_i. \tag{4.2}$$

The repeated indices indicate the usual summation. Equations (2.1), (3.1), (4.1) and (4.2) specify the kinematics of the dynamical system.

The thermodynamic force vector, F_i, is defined such that

$$\dot{\Phi} + \int F_i J_i \, dV = 0 \tag{4.3}$$

for any virtual flux satisfying the kinematics. The integral extends over the *volume* of the second phase. The equivalence of the present approach to the local chemical potential concepts of Herring (1950) is demonstrated in Appendix C. The kinetics are prescribed by

$$J_i = M_v F_i, \tag{4.4}$$

where M_v is the mobility of the solid molecules in the liquid phase. This phenomenological quantity must be determined by experiments.

Equations (4.3) and (4.4) are equivalent to the following variational principle. Of all virtual fluxes satisfying the kinematics, the actual flux minimizes the functional

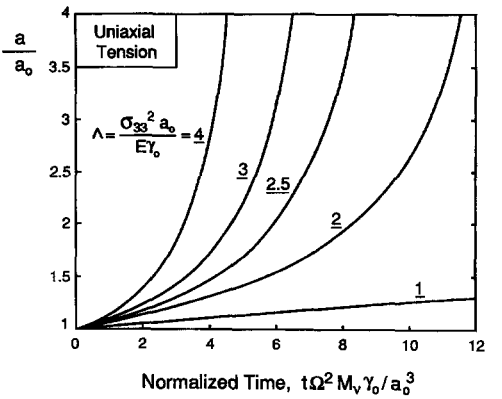

Fig. 10. Evolution of the semi-axis of the void due to diffusion in the fluid inside the void.

$$\Pi = \dot{\Phi} + \int \frac{J_i J_i}{2M_v} \mathrm{d}V. \tag{4.5}$$

The characteristic time is found to be

$$t_0 = \frac{a_0^3}{\Omega^2 M_v \gamma_0}. \tag{4.6}$$

For the following calculation, we select a particular flux pattern

$$[J_1, J_2, J_3] = \frac{1}{\Omega}\frac{\dot{\alpha}}{\alpha}[-X, -Y, 2Z]. \tag{4.7}$$

This pattern satisfies the kinematics [(2.1), (3.1), (4.1) and (4.2)], and is therefore a valid choice according to the variational principle. The pattern is also consistent with intuition about diffusion in a fluid. Notably, when $\dot{\alpha} > 0$, atoms diffuse in the directions sketched in Fig. 1(c), so that the spheroid elongates along the X-axis and shrinks along the Z-axis. The normalized functional Π for this flux pattern is

$$\Pi = (-\Lambda I_0 + I_1)\dot{\alpha} + \tfrac{1}{2} I_3 \dot{\alpha}^2. \tag{4.8}$$

The coefficients I_i are listed in Appendix A.

Minimizing Π by letting $\partial\Pi/\partial\dot{\alpha} = 0$ gives

$$\dot{\alpha} = (\Lambda I_0 - I_1)/I_3. \tag{4.9}$$

This equation is integrated to give the evolution of the semi-axis, Fig. 10. A comparison between Figs 7 and 10 indicates that the shape changes are qualitatively similar for the two kinetic processes. Yet, the time scales, (3.6) and (4.6), can be very different. The mobility in the fluid is often much higher than the mobility along the void surface, leading to faster void shape change.

5. SURFACE REACTIONS

The kinetic problem is formulated by following general procedure of non-equilibrium thermodynamics (Prigogine, 1967). The system is in equilibrium thermally with an infinite heat bath at temperature T and mechanically with the external stress. Only the chemical equilibrium is not reached. Denote $\dot{\xi}$ as the reaction rate (i.e. the number of solid molecules per time deposited on unit area of the surface). Mass conservation requires that the surface recedes at velocity

$$V_n = -\dot{\xi}\Omega. \tag{5.1}$$

Equations (2.8), (3.1) and (5.1) specify the kinematics of the evolution.

Define the affinity, A, as the reduction in the free energy associated with depositing one solid molecule onto the void surface. Thus,

$$\dot{\Phi} + \int A\dot{\xi}\,\mathrm{d}S = 0 \tag{5.2}$$

for any virtual distribution of the reaction rate. The integration extends over the solid surface participating in the reaction. The second term is the rate of dissipation, so that this definition is a statement of energy balance. The energy rate is never positive and the dissipation rate is never negative (A and $\dot{\xi}$ always have the same sign).

The affinity in general is nonuniform on the surface and a function of position. For crystals having isotropic surface tension, the affinity is calculated as follows. The time rate of the free energy is

$$\dot{\Phi} = -\int [\gamma_0\kappa + w + \sum(\mu_s^0 + \nu_i\mu_i)/\Omega]\, V_n\,\mathrm{d}S. \tag{5.3}$$

Here, w is the strain energy density on the void surface and κ is the curvature of the void surface ($\kappa = -2/a$ for a spherical void of radius a). This equation is derived from the definition of the free energy, (2.11). Inserting (5.3) into (5.2) and asserting its validity for arbitrary virtual V_n and $\dot{\xi}$ satisfying kinematic equation (5.1), we obtain that

$$A = -(\gamma_0\kappa + w)\Omega - \sum(\mu_s^0 + \nu_i\mu_i). \tag{5.4}$$

The affinity has the dimension of the chemical potential (energy per solid molecule). The solid precipitates onto the void surface when $A > 0$ and dissolves from the surface when $A < 0$. The reaction stops when $A = 0$.

The reaction rate is assumed to be locally determined by the affinity. When the reaction proceeds close to equilibrium, the affinity is much smaller than the average thermal energy of a molecule, $|A|/\kappa T \ll 1$. Under this condition, the reaction rate $\dot{\xi}$ varies linearly with the affinity A:

$$\dot{\xi} = LA. \tag{5.5}$$

The kinetic coefficient L depends on the temperature and the specific chemical reaction, but is independent of A. It is used here as a phenomenological constant, to be

determined empirically by its macroscopic consequences. In the molecular picture, L relates to the frequency at which the gas molecules strike the solid surface, the fraction of the active sites on the surface and the energy barrier between the reactants and the products. The special case vaporization–condensation of monatomic solids is summarized in Appendix D.

A variational principle is identified to replace (5.2) and (5.5). Of all virtual distributions of the reaction rate $\dot{\xi}$, the actual one minimizes

$$\Pi = \dot{\Phi} + \int \frac{\dot{\xi}^2}{2L} \mathrm{d}S. \tag{5.6}$$

At a given time, the system configuration is fixed and only the reaction rate, $\dot{\xi}$, varies in this variational principle. Once the rate is determined, the configuration updates accordingly for a small time step. The procedure is repeated for many steps.

A characteristic time may be defined as

$$t_0 = \frac{\gamma_0 E^2}{\sigma_{33}^4 \Omega^2 L}. \tag{5.7}$$

For an evolution path approximated by a sequence of spheroids, the surface velocity determined from (2.8) and (3.1) is

$$V_n = (\dot{a}c\cos^2\theta + a\dot{c}\sin^2\theta)\,\mathrm{d}\theta/\mathrm{d}s, \tag{5.8}$$

where $\mathrm{d}s$ is the line element of the ellipse on the (X, Z) plane. Normalizing the time by t_0 of (5.7), the semi-axes by λ of (2.13) and the free energy by $4\pi\lambda^2\gamma_0$, the functional takes the form

$$\Pi = -f_a\dot{a} - f_c\dot{c} + \tfrac{1}{2}H_{aa}\dot{a}^2 + \tfrac{1}{2}H_{cc}\dot{c}^2 + H_{ac}\dot{a}\dot{c}. \tag{5.9}$$

The dimensionless coefficients are give in Appendix A. Note that

$$f_a = -\partial\Phi/\partial a, \quad f_c = -\partial\Phi/\partial c \tag{5.10}$$

are the generalized forces associated with the semi-axes a and c. Setting $\partial\Pi/\partial\dot{a} = 0$ and $\partial\Pi/\partial\dot{c} = 0$, one obtains

$$\begin{bmatrix} H_{aa} & H_{ac} \\ H_{ac} & H_{cc} \end{bmatrix} \begin{bmatrix} \dot{a} \\ \dot{c} \end{bmatrix} = \begin{bmatrix} f_a \\ f_c \end{bmatrix} \tag{5.11}$$

Evidently, the elements of the matrix H should be interpreted as the generalized viscosities. The set of nonlinear differential equations are integrated numerically.

The evolution paths are superimposed in Fig. 6 by dotted curves for several initially spherical voids ($\eta = 0$, uniaxial stress). The void of initial radius λ changes shape and shrinks. The voids of radii 1.5λ and 2λ evolve to penny-shaped cracks. The semi-axes

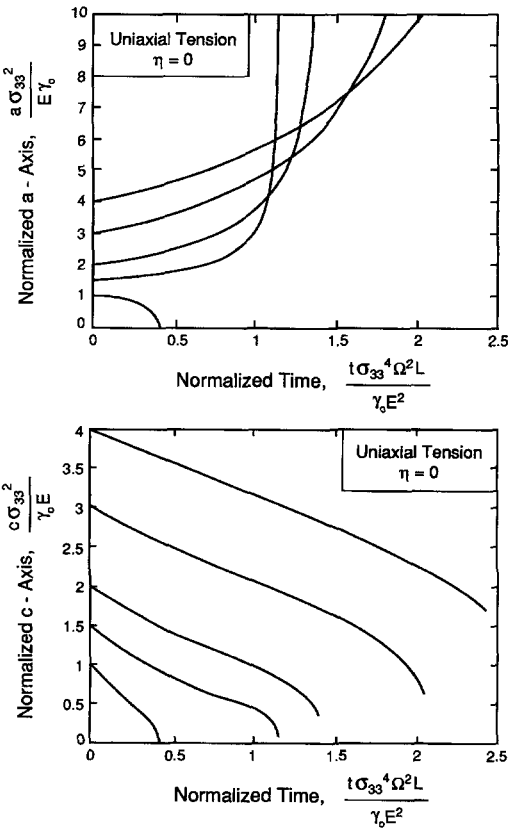

Fig. 11. Evolution of the semi-axes of the void due to surface reaction.

as functions of time are plotted in Fig. 11. We have also simulated the cases $\eta = -1$ and $\eta = +1$ and found no qualitative change in the behaviors.

6. COMPARISON WITH EXPERIMENTS

In this section, we compare the theoretical predictions with the experimental data on sapphire. Sapphire does not creep appreciably below 1600°C and it fractures instantaneously on application of a stress exceeding a limiting value. Stresses below this limit may also cause fracture if maintained for a sufficient duration. This time-to-fracture increases as either the stress or the temperature decreases, and appears to approach infinity at a *threshold stress*. Such time dependence also causes the fracture strength to increase with increasing strain rate. Newcomb and Tressler (1993) measured the tensile strength of sapphire fibers subject to different strain rates at 800–1500°C. Visible on fracture surfaces are circular crack-like features surrounding the pores (Fig. 12). Similar features were also reported by Rice and Becher (1977) and Firestone and Heuer (1976). These crack-like features grow slowly up to a critical

Fig. 12. A high temperature fracture surface for a sapphire fiber. The void that initiated the failure is at the center. Around the void is a relatively planar region, which coincides with the diffusive shape change that precedes failure.

Table 1. *Data for single crystal α-Al_2O_3 (sapphire) at 1200–1600°C*

Molecular volume	$\Omega = 4.25 \times 10^{-29}$ m^3 molecule^{-1}
Young's modulus	$E = 405$ GPa (Goto and Anderson, 1988)
Surface energy	$\gamma_s = 2.559 - 0.784 \times 10^{-3} T$ (Jm^{-2}) (Nikolopoulos, 1985)
Surface diffusivity	$D_s\delta_s = 1.2 \times 10^{-10} \exp(-338(\text{kJ mole}^{-1})/RT)$ m^{3}s^{-1} (Tsoga and Nikolopoulos, 1994)

size, leading to catastrophic fracture. In what follows, we will assume that surface diffusion is the mass transport mechanism. The basic material data to be used are listed in Table 1. Note that the surface diffusivity is averaged from the data compiled by Tsoga and Nikolopoulos (1994).

Note that the fracture energy of sapphire is anisotropic. It is impossible to cause cleavage on the basal plane. A crack introduced on the basal plane zigzags, propagating largely on rhombohedral planes in such a way that the macroscopic fracture surface is approximately parallel to the basal plane. Given this and the crude way in using (3.13), it is difficult to accurately assign a value for G_c. The value $G_c/\gamma_0 = 3.5$ is used in this comparison. The experimental data of Newcomb and Tressler at 1500°C are plotted in Fig. 13. To match the *scale* of the prediction with the data, the stress-like parameter was fit to be

$$(E\gamma_0/a_0)^{1/2} = 471 \text{ MPa}, \tag{6.1}$$

and the characteristic strain rate

$$\dot{\varepsilon}_0 = 7 \times 10^{-2} \text{ min}^{-1}. \tag{6.2}$$

The curve on Fig. 13 is the theoretical prediction (Fig. 9) plotted again using the values (6.1) and (6.2). The theory predicts a threshold stress below which the fiber will never fracture for indefinitely low strain rates. Evidently, this threshold corresponds to the limit point $\Lambda_c = 0.91$ in Fig. 4.

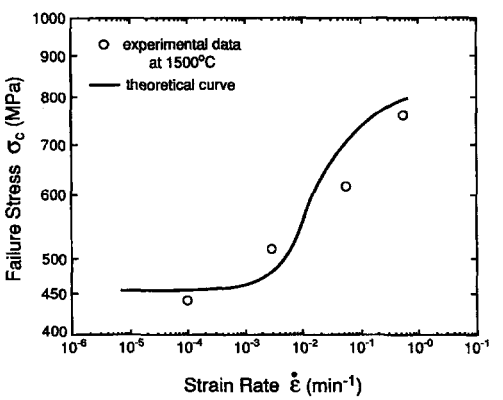

Fig. 13. The theoretical curve plotted to best fit the experimental data at 1500°C.

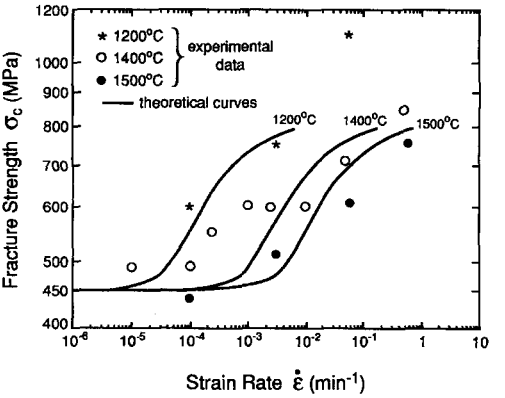

Fig. 14. Comparison between experimentally and theoretically determined strength/strain-rate curves.

Within the temperature range of interest, the stress-like parameter (6.1) is taken to be temperature independent and the strain rate parameter obeys the Arrhenius law

$$\dot{\varepsilon}_0 = \beta \exp(-Q/RT), \tag{6.3}$$

where $R = 8.31\ JK^{-1}\ mole^{-1}$ is the gas constant, and $Q = 338\ kJ\ mole^{-1}$ is chosen to be the same as the activation energy of surface diffusion (Table 1). The frequency factor determined from (6.2) is $\beta = 6.4 \times 10^8\ min^{-1}$ and is assumed to be independent of the temperature. The predicted curves at 1200 and 1400°C, using the same parameters determined above, are plotted in Fig. 14. Also included for comparison are the experimental data of Newcomb and Tressler (1993). The agreement is encouraging.

Comparisons can be made with the basic materials data in Table 1. First, the experimentally determined threshold strength, $\sigma_{th} \approx 450$, can be compared with the limit point on Fig. 4. Using an initial pore radius $a_0 = 2\ \mu m$, the calculated dimensionless ratio (2.5), $\Lambda = 0.83$, is close to the predicted limit point on Fig. 4 under uniaxial tension, $\Lambda_c = 0.91$. This comparison involves only the energetics of the theory.

Next we compare the kinetics. The characteristic strain rate calculated from (3.12) using the data in Table 1 and $a_0 = 2\ \mu m$, $\dot{\varepsilon}_0 \approx 10^{-7}\ min^{-1}$ at 1500°C, is low compared with the best fit to the strength/strain-rate curve (6.2). There are several reasons for the disagreement. First, the surface diffusivity reported in the literature varies by several orders of magnitude and is sensitive to surface contamination. Second, the environment in the pores is unknown. Evaporation–condensation may be the dominant kinetic process (Stevens and Dutton, 1971), because sapphire can form gaseous suboxides at moderate temperatures. The reliable kinetic data needed to evaluate this mechanism are unavailable. Third, to simplify the calculation, we have assumed that the pores evolve as a sequence of spheroids. This approximation is expected to be adequate when Λ is only slightly higher than Λ_c and when the time is short. However, for larger Λ or long time, surface diffusion would cause the pore shape to deviate significantly from a spheroid. Such crack-like features would extend much faster than the present analysis would predict.

Newcomb and Tressler (1993) interpreted their experimental observations on the

basis of thermally activated bond rupture at the crack front. The main drawback with this interpretation is that it does not explain how an atomistically sharp crack can nucleate from a residual pore in the first place. It is most probable that the a pore changes shape by the mass transport processes considered here. Thus, once a crack-like feature has emerged, rapid growth proceeds by thermally-activated bond rupture. Notice, however, that the emergence of a crack-like feature, rather than its growth, takes the major portion of the time-to-fracture (Fig. 8).

In summary, the theory predicts the correct trends. Once the *scales* of the theoretical curves are fixed by the experimental data at one temperature, the theoretical curves at other temperatures agree well with the remaining experimental data. The theory predicts a threshold strength consistent with experiment. The characteristic strain-rate differs by several orders of magnitude between the theoretical prediction and the experimental data. Finally, it is noted that mass transport processes operate under both tensile and compressive stress, because the stress enters only through elastic energy. By contrast, crack-front bond rupture requires tensile stress. It may therefore be worthwhile to carry out compressive tests to discriminate the two classes of mechanisms. If mass transport processes operate, crack-like features would grow from pores even under compression. A subsequent tension test would then cause instantaneous fracture at a lower stress.

ACKNOWLEDGMENTS

The study of surface reaction was initiated at a suggestion of Professor F. F. Lange. The work was supported by the Defense Advanced Research Projects Agency through the University Research Initiative under the Office of Naval Research contract N-0014-92-J-08, and by the National Science Foundation through grant MSS-9202165 and a Young Investigator Award MSS-9258115 to Z. Suo.

REFERENCES

Asaro, R. J. and Tiller, W. A. (1972) Interface morphology development during stress corrosion cracking: part I. Via surface diffusion. *Metall. Trans.* **3**, 1789–1796.

Chan, K. S. and Page, R. A. (1993) Creep damage development in structural ceramics. *J. Am. Ceram. Soc.* **76**, 803–826.

Chiu, C.-H. and Gao, H. (1993) Stress singularities along a cycloid rough surface. *Int. J. Solids Struct.* **30**, 2983–3010.

Eshelby, J. D. (1957) The determination of the elastic field of an spheroidal inclusion, and related problems. *Proc. R. Soc. Lond. A* **241**, 376–396.

Firestone, R. F. and Heuer, A. H. (1976) Creep deformation of 0° sapphire. *J. Am. Ceram. Soc.* **59**, 34–29.

Freund, L. B. and Jonsdottir, F. (1993) Instability of a biaxially stressed thin film on a substrate due to material diffusion over its free surface. *J. Mech. Phys. Solids.* **41**, 1245–1264.

Gao, H. (1991) Morphological instabilities along surfaces of anisotropic solids. *Modern Theory of Anisotropic Elasticity and Applications* (ed. J. J. Wu, T. C. T. Ting and D. M. Barnett), pp. 139–150. SIAM, Philadelphia, PA.

Gao, H. (1992) Stress analysis of holes in anisotropic elastic solids: conformal mapping and boundary perturbation. *Q. J. Mech. Appl. Math.* **45**, 149–168.

Gao, H. (1993) The hypocycloid cavity: a path from a Griffith slit crack to a cusped cycloid surface. *Proc. R. Soc. Lond. (submitted)*.
Goto, T. and Anderson, O. L. (1988) Apparatus for measuring elastic constants of single crystals by a resonance technique up to 1825 K. *Rev. Sci. Instrum.* **59**, 1405–14.
Grinfel'd, M. A. (1986) Instability of the separation boundary between a non-hydrostatically stressed elastic body and a melt. *Sov. Phys. Dokl.* **31**, 831–834.
Grinfel'd, M. A. (1993) The stress driven instability in elastic crystals: mathematical models and physical manifestations. *J. Nonlinear Sci.* **3**, 35–83.
Herring, C. (1950) Diffusional viscosity of a polycrystalline solids. *J. Appl. Phys.* **21**, 437–445.
Mullins, W. W. (1957) Theory of thermal grooving. *J. Appl. Phys.* **28**, 333–339.
Newcomb, S. A. and Tressler, R. E. (1993) Slow crack growth in sapphire fibers at 800° to 1500° C. *J. Am. Ceram. Soc.* **76**, 2505–2512.
Nikolopoulos, P. (1985) Surface, grain-boundary and interfacial energies in Al_2O_3 and Al_2O_3–Sn, Al_2O_3–Co systems. *J. Mater. Sci.* **20**, 3993–4000.
Prigogine, I. (1967) *Introduction to Thermodynamics of Irreversible Processes*, 3rd edn. Wiley, New York.
Rice, R. W. and Becher, P. F. (1977) Comment on "creep deformation of 0° sapphire" *J. Am. Ceram. Soc.* **60**, 186–188.
Stevens, R. N. and Dutton, R. (1971) The propagation of Griffith cracks at high temperatures by mass transport processes. *Mater. Sci. Engng* **8**, 220–234.
Spencer, B. J., Voorhees, P. W. and Davis, S. H. (1991) Morphological instability in epitaxially strained dislocation-free solid films. *Phys. Rev. Lett.* **67**, 3696–3699.
Srolovitz, D. J. (1989) On the stability of surfaces of stressed solids. *Acta Metall.* **37**, 621–625.
Suo, Z. and Wang, W. (1994) Diffusive void bifurcation in stressed solid. *J. Appl. Phys.* (submitted).
Tada, H., Paris, P. and Irwin, G. (1985) *The Stress Analysis of Cracks Handbook*. Del Research Corporation, St. Louis, MO.
Tsoga, A. and Nikolopoulos, P. (1994) Groove angles and surface mass transport in polycrystalline alumina. *J. Am. Ceram. Soc.* **77**, 954–960.
Yang, W. H. and Srolovitz, D. J. (1993) Cracklike surface instabilities in stressed solids. *Phys. Rev. Lett.* **71**, 1593–1596.

APPENDIX A: NOTES ON DIMENSIONLESS COEFFICIENTS

The increase of the strain energy upon introducing a traction-free spheroidal void into an infinite solid was computed by following the method of Eshelby (1957). The coefficient in (2.2) is

$$B = \tfrac{1}{2}(2k^2C_{11} + 2kC_{13} + kC_{31} + C_{33})$$

and

$$C_{11} = \frac{(1-S_{33})(1-v) - 2vS_{13}}{\Delta}$$

$$C_{13} = \frac{S_{13} - (1-S_{33})v}{\Delta}$$

$$C_{31} = \frac{2S_{31}(1-v) - 2v(1-S_{11}-S_{12})}{\Delta}$$

$$C_{33} = \frac{1-S_{11}-S_{12}-2vS_{31}}{\Delta}$$

$$\Delta = (1-S_{33})(1-S_{11}-S_{12})-2S_{31}S_{13}.$$

All S_{ij} can be found in Eshelby (1957).

The surface energy U_s was calculated by integrating the surface tension over the spheroid surface. The coefficients in (2.3) and Appendix B are

$$A_0 = \frac{\alpha^2}{2} + \frac{\ln(\sqrt{\alpha^6-1}+\alpha^3)}{2\alpha\sqrt{\alpha^6-1}}$$

$$A_1 = \int_0^{\pi/2} \frac{\cos^3\theta}{\alpha\sqrt{\alpha^6\sin^2\theta+\cos^2\theta}}\,d\theta$$

Numerical integration was used to evaluate the coefficients in this appendix when needed.

The coefficients in (3.9) and (4.8) are given by

$$I_0 = dB/d\alpha, \quad I_1 = dA_0/d\alpha$$

$$I_2 = \frac{1}{4\alpha^2}\int_0^{\pi/2} \sin^2 2\theta\sqrt{\sin^2\theta+\alpha^{-6}\cos^2\theta}\cos\theta\,d\theta$$

$$I_3 = \tfrac{4}{15}(1+\alpha^{-6})$$

In evaluating coefficients in (5.9), the normalized energies are

$$U_E = \tfrac{1}{6}a^2c\,(2k^2C_{11}+2kC_{13}+kC_{31}+C_{33})$$

$$U_S = \frac{ac}{2}\left[(a/c)+\frac{\ln(\sqrt{(a/c)^2-1}+(a/c))}{\sqrt{(a/c)^2-1}}\right]$$

$$U_C = -\tfrac{1}{3}\eta a^2c$$

The coefficients in (5.9) are given by

$$H_{aa} = \int_0^{\pi/2} \frac{ac^2\cos^5\theta\,d\theta}{\sqrt{a^2\sin^2\theta+c^2\cos^2\theta}}$$

$$H_{cc} = \int_0^{\pi/2} \frac{a^3\sin^4\theta\cos\theta\,d\theta}{\sqrt{a^2\sin^2\theta+c^2\cos^2\theta}}$$

$$H_{ac} = \int_0^{\pi/2} \frac{a^2c\sin^2\theta\cos^3\theta\,d\theta}{\sqrt{a^2\sin^2\theta+c^2\cos^2\theta}}$$

APPENDIX B: INFLUENCE OF SURFACE ENERGY ANISOTROPY ON VOID INSTABILITY

Let γ_0 be the surface tension of the crystal plane normal to the Z-axis, Fig. 1(a), and $(1+g)\gamma_0$ be the surface tension of the crystal plane normal to the X-axis. Denote ϕ as the angle from the Z-axis to the surface normal $\mathbf{n}$. The surface tension for an arbitrary crystal plane is interpolated by

$$\gamma = \gamma_0(1+g\sin^2\phi).$$

The total surface energy is obtained by integrating γ over the void surface. Thus,

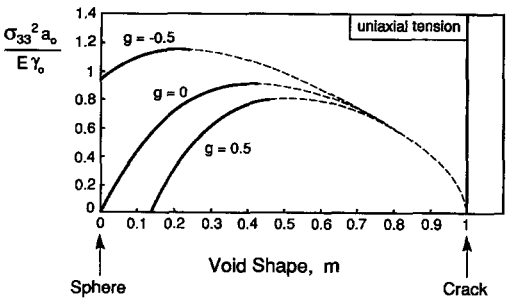

Fig. B1. The effect of surface energy anisotropy on the equilibrium states.

$$U_s = 4\pi a_0^2 \gamma_0 (A_0 + gA_1).$$

The coefficients A_0 and A_1 are given in Appendix A.

The equilibrium states of a void under uniaxial stress σ_{33} for several values of anisotropy factor g are plotted in Fig. B1. When $g > 0$, the surface tension is smallest in the crystal plane normal to the loading axis, so that the anisotropy decreases the limit load. When $g > 0$, the surface tension is largest in the crystal plane normal to the loading axis, so that the anisotropy increases the limit load. Note that all curves merge to the same asymptote when $m \to 1$, as governed by (2.7).

APPENDIX C: COMPARISON OF VARIATIONAL PRINCIPLE APPROACH WITH CHEMICAL POTENTIAL APPROACH

Consider a void in an isotropic crystal. Denote w as the strain energy per volume and γ_0 the surface energy per area. The free energy rate is given by

$$\dot{\Phi} = -\int (\gamma_0 \kappa + w) V_n \, dS. \tag{C1}$$

Following the usual convention, define the chemical potential on the surface as

$$\mu = \Omega(\gamma_0 \kappa + w). \tag{C2}$$

The chemical potential in the volume of the liquid is yet to be determined. Replacing V_n by J (4.2), the free energy rate becomes

$$\dot{\Phi} = \int \mu J_i n_i \, dS. \tag{C3}$$

Consequently, the surface value of the chemical potential is simply the free energy increase associated with adding one atom to the surface. Extend μ into the volume of the liquid and (C3) can be converted into an integral over the volume of the liquid by using the divergence theorem. Together with (4.1), the result is

$$\dot{\Phi} = \int \mu_{,i} J_i \, dV. \tag{C4}$$

Inserting (C4) into (4.3) and asserting its validity for *arbitrary* flux vector, one finds that

$$F_i = -\mu_{,i} \tag{C5}$$

holds for every point in the liquid. That is, the driving force is derived from the potential, μ.

Equations (4.1) and (C5), together with the kinetic relations, imply that μ satisfies the Laplace equation.

According to this approach, the void evolution would be traced as follows. For a given void shape, the elasticity problem is solved to prescribe the boundary value of μ from (C2). The value of μ inside the liquid is then solved from the Laplace equation. The flux and the surface velocity are determined and used to update the void shape. The procedure is repeated for many time steps.

APPENDIX D: VAPORIZATION–CONDENSATION OF A MONATOMIC SYSTEM

Following Mullins (1957), we now derive the coefficient L, defined by (5.5), from the kinetic theory of perfect gases, for vaporization–condensation of a *monatomic* system. The model assumes that the deposition rate is governed entirely by the collision rate. That is, an atom joins the solid if it hits the surface: no energy barrier exists. Its applicability to more complex systems is questionable. For example, even in the absence of elements other than oxygen and aluminum, sapphire (Al_2O_3) forms gaseous suboxides (Al_2O_2 and Al_2O) at moderate temperatures. Condensation is a sequence of reactions involving active sites and energy barriers. For a complex surface reaction near an equilibrium state, the linear kinetic coefficient L can be determined by experiments such as thermal grooving, provided other mass transport processes are sufficiently slow. The following derivation only serves to illustrate the connection between this article and Mullins (1957).

Consider an unstressed, flat, monatomic solid surface in contact with its own vapor at pressure p. For this special case, the affinity of (5.4) reduces to

$$A = -\mu_s^0 + \mu_v^0 + kT \ln (p/p^0). \tag{D1}$$

The subscripts s and v indicate the solid and the vapor. The minus sign is removed for the vapor because it is the "reactant". Let the equilibrium vapor pressure over a flat, unstressed solid surface be p^∞. This equilibrium is reached when the affinity vanishes, namely

$$-\mu_s^0 + \mu_v^0 + kT \ln (p^\infty/p^0) = 0. \tag{D2}$$

Consequently, for the solid in contact with its own vapor whose pressure p differs slightly from p^∞, the affinity can be expressed by

$$A = kT \ln \left(\frac{p}{p^\infty}\right) \approx kT \frac{p-p^\infty}{p^\infty}. \tag{D3}$$

The approximation is valid when $|p-p^\infty|/p^\infty \ll 1$, or $|A|/kT \ll 1$.

The kinetic theory of gases shows that the number of vapor atoms impinging on the solid surface per time per area is

$$p(2\pi mkT)^{-1/2}, \tag{D4}$$

where m is the mass per atom. When the solid surface is in equilibrium with its vapor, $p = p^\infty$, the flux of atoms emitting from the surface just balances the flux of the impinging atoms. Consequently, the solid emits

$$p^\infty (2\pi mkT)^{-1/2} \tag{D5}$$

atoms per time per area. When $p \neq p^\infty$, the net flux deposited on the surface is

$$\dot{\xi} = (p-p^\infty)(2\pi mkT)^{-1/2}. \tag{D6}$$

A comparison among (D3), (D6) and $\dot{\xi} = LA$ gives

$$L = \frac{p^\infty}{(2\pi m)^{1/2}(kT)^{3/2}}. \tag{D7}$$